

Received July 14, 2018, accepted September 11, 2018, date of publication October 1, 2018, date of current version December 3, 2018.

Digital Object Identifier 10.1109/ACCESS.2018.2872797

# Automated Analysis of Meshing Performance of Harmonic Drive Gears Under Various Operating Conditions

DONGHUI MA, (Student Member, IEEE), RUI WANG, PENGFEI RAO, RUOMIN SUI, AND SHAOZE YAN 

State Key Laboratory of Tribology, Department of Mechanical Engineering, Tsinghua University, Beijing 100084, China

Corresponding author: Shaoze Yan (yansz@mail.tsinghua.edu.cn)

This work was supported in part by the Beijing Natural Science Foundation under Grant 3172017 and in part by the National Natural Science Foundation of China under Grant 11872033 and Grant 11272171.

**ABSTRACT** Accurate and efficient analysis of the meshing performance of harmonic drives (HDs) is the core and challenging problem for the improvement of the positioning accuracy of robots. This paper presents an integrated hardware and software system for an automated analysis of the meshing performance of the HD under various operating conditions. First, an optical measurement method based on the principle of periscope is proposed to capture the meshing images at a different driving speed and load torque. Next, a position tracking algorithm based on image processing and pattern recognition is designed to obtain the positions of the flexspline and circular spline teeth in the meshing process. Furthermore, a mathematical model based on the geometric relationship between the flexspline and the circular spline teeth is established to calculate the meshing backlash and depth. Last, the performance and advantages of the proposed method are demonstrated through uncertainty analysis and comparing with the conventional method. The results show that the error of the calculated meshing parameters is close to 0, and 1.59 s are required to track the FS teeth in each video frame with a laptop of 2.6-GHz CPU and 12-GB RAM. Moreover, the total rotation angle of the wave generator and the backlash and depth in the meshing process are seriously affected by the driving speed and load torque. Our method offers an effective tool for the HD manufacturers to examine the quality of products, and the obtained results can help to optimize the tooth profile of the HD.

**INDEX TERMS** Harmonic drive gear, meshing performance, operating condition, computer vision, pattern recognition.

## I. INTRODUCTION

Harmonic drive (HD), a novel mechanical transmission element invented in the 1950s [1], has been one of the key components of the industrial and space robots [2]–[5]. The HD is usually considered to have zero backlash [6]–[9]. Actually, the minimum backlash of the HD in the meshing process is nonzero and affected by the operating conditions [10], [11], which results in the decline of the robot positioning accuracy [12], [13]. Current methods are mainly used to calculate the meshing parameters of the HD under no-load condition [14]. Thus, how to accurately and efficiently analyze the meshing performance of the manufactured HD under various operating conditions, is one of the key technique problems in the HD industry.

In the past six decades, three theoretical methods for the meshing analysis of the HD have been suggested, namely

the classical envelope method, the centrode method, and the graphic method [10], [15]–[17]. Among the three methods, the classical envelope method possesses high precision and is easy to be programmed [16]. In order to improve the computational efficiency of the classical envelope method, Xin [18] proposed a modified kinematics method through establishing a matrix which contains only the kinematics parameters of the flexspline (FS). For a specific kind of the wave generator (WG), the matrix keeps constant when the tooth profile of the HD changes, and this method is usually used to investigate the meshing characteristics of the HD with different tooth profiles [19]. Moreover, since the rotation angle of the symmetric line of the FS tooth relative to its position vector and the rotation angle caused by the circumferential deformation of the FS are simplified in the classical envelope method, Yang *et al.* [20] proposed an improved

envelope method to obtain a more precise solution of the conjugate profiles of the HD, and the accuracy and effectiveness of the proposed method were verified by the finite element analysis (FEA). Besides, since the conventional centrode method is only suitable for the planar meshing analysis of the HD, Dong [15] proposed an improved centrode method based on the spatial deformation of the FS, and investigated the planar and spatial kinematics characteristics of the HD under no-load condition [21], [22]. In addition to the above methods, Wang *et al.* [23] proposed a rack approximation method based on the assumption that the teeth number of the FS and circular spline (CS) are infinite, and designed the S-type tooth profile of the HD [24]. What's more, Ivanov [10] first revised the ideal deformation equation of the FS based on the measured radial displacement under loading condition, and then established a kinematics model to investigate the effects of the load torque on the meshing performance of the HD. The FEA methods are also used for the meshing analysis of the HD. Chen *et al.* [11] established a simplified FEA model to investigate the distribution and magnitude of the meshing backlash of the HD with the double-circular-arc common-tangent tooth profile. Leon *et al.* [25] examined the influences of the pressure angle, modulus and tooth correction factor on the transmission performance of the HD based on the FEA and full-factorial experimental design methods. Furthermore, Sahoo and Maiti [26], [27] estimated the load shared by the meshed teeth pairs of the HD in the meshing process based on the FEA method, and the calculated results were in agreement with the experimental ones.

Although the theoretical and FEA methods are very convenient for the meshing analysis of the HD, they have some limitations. As is known to us, the gear engagement of the HD is realized through the elastic deformation of the FS, and thus the accuracies of the theoretical methods mainly depend on the precision of the established deformation model of the FS. However, the deformation characteristics of the FS are usually affected by the driving speed, output load, ambient temperature and other operating parameters, which have not been fully revealed up to now [15], [28], [29]. Moreover, in the existing FEA models of the HD, the flexible bearing of the WG is usually ignored, and the load and contact property are set according to the empirical formula because the load distribution and friction behavior among the meshed teeth pairs are still not clear [28], [30]–[33]. Consequently, experimental methods are required to reveal the effects of the operating conditions on the meshing performance of the HD and improve the existing theoretical and FEA methods. However, the internal gear transmission mode and the extremely small module make it very difficult to measure the meshing process of the HD, and the general experimental techniques for the rigid gear transmission are not directly applicable [10]. Wang *et al.* [19] used a microscope to observe the meshing state of the HD at different time. Unfortunately, the quality of the acquired meshing images of the HD was not high enough to quantitatively analyze the meshing characteristic of the HD, and a large amount of human effort was needed to record

the whole meshing process of the HD under different working conditions. Ma *et al.* [14] proposed a vision-based method to investigate the effects of the driving speed on the kinematics characteristics of the HD using a high speed camera (HSC), and the effectiveness and advantages of the proposed method were validated by the uncertainty analysis and comparing with the theoretical results. Nevertheless, this approach has two shortcomings. First, the experimental apparatus can only be used to measure the meshing process of the HD under no-load condition. Second, the positions of the FS and CS teeth in the meshing process were detected manually. Based on the above analyses, it is meaningful to utilize an optical measurement method to accurately measure the meshing process of the HD under various operating conditions. More importantly, the artificial intelligence should be applied to automatically process the obtained meshing images of the HD so that the amount of human effort can be reduced and the human errors can be avoided.

This paper presents a pioneer study of automatically analyzing the meshing performance of the HD under various operating conditions. A framework for acquiring the meshing images, tracking the meshed teeth pairs and calculating the meshing parameters of the HD is developed. First, an optical measurement method based on the principle of periscope is proposed to measure the meshing process of the HD at different driving speed and load torque. Next, a position tracking algorithm based on image processing and pattern recognition is designed to obtain the positions of the FS and CS teeth in the meshing process. Further, a mathematical model based on the geometric relationship between the FS and CS teeth is established to calculate the meshing backlash and depth. Last, the computational accuracy and efficiency of the proposed method are discussed, and its effectiveness and advantages are demonstrated through comparing with the conventional method. The results show that the proposed method maybe an effective tool for manufacturers to examine the meshing performance of the HD. In addition, the obtained meshing characteristics of the HD under various operating conditions can help to improve the theoretical methods and design new tooth profiles.

The rest of the paper is organized as follows. The meshing principle of the HD and the theoretical method for calculation of the meshing backlash and depth are introduced in Section II. The framework of the proposed method and the implementation of each phase are presented in Section III. The performance of the proposed method is evaluated in Section IV. The results obtained by the proposed and theoretical methods are compared in Section V. Conclusions are given in Section VI.

## II. THEORY

### A. STRUCTURE AND THE PRINCIPLE OF OPERATION OF THE HD

A normal HD is composed of a WG, a CS, and a FS. As shown in Fig. 1(a), the WG is an elliptical cam equipped with a

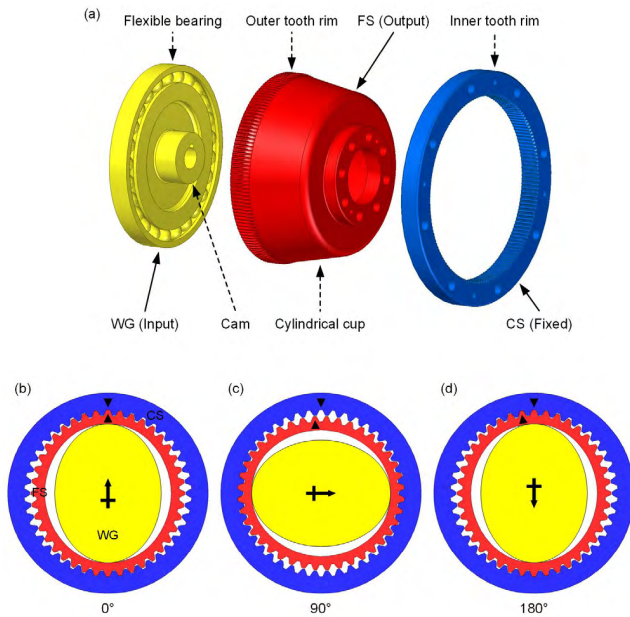


**FIGURE 1.** Structure and the principle of operation of a normal HD. (a) Basic components of the HD; (b) Relationship between the meshing period of the HD and the rotating period of the double-wave WG.

flexible bearing, the CS is a rigid gear equipped with an inner tooth rim, and the FS is a cylindrical cup equipped with an outer tooth rim at its open end [34]. In the assembly state, the WG is inserted into the FS and driven by the motor, the closed end of the FS is connected with the loader, and the CS is installed above the tooth rim of the FS and remains stationary. In the transmission state, the WG keeps rotating in the FS, the FS deforms continuously and meshes with the CS, and the reverse rotation relative to the WG is obtained on the loader shaft. For the HD with the double-wave WG, when the teeth number of the FS is two fewer than that of the CS, the meshing period of the HD is half of the rotating period of the WG [10], which can be seen in Fig. 1(b)-(d).

**B. PARAMETERS FOR CHARACTERIZING THE MESHING PERFORMANCE**

The meshing backlash and depth are two key indexes to evaluate the meshing performance of the HD [10], [35]. As show in Fig. 2(a), the FS tooth meshes with the CS tooth in the engaging-in phase. The midpoint A on the addendum of the FS tooth is denoted by the black circle, and its trajectory is marked with the red curve. It is shown that the meshing backlash varies with the position of the FS tooth in the meshing process, and researchers have proved that the meshing backlash near the addendum of the FS tooth is usually smaller than that near the addendum of the corresponding CS tooth [10], [16]. Thus, the meshing backlash is defined as the circumferential distance between the tooth profiles of the FS and CS teeth at the endpoint on the addendum of the FS tooth [16]. In addition, in this figure, the meshing backlash  $j_{in}$  on the engaging-in arc is defined as the circumferential

distance between the right endpoint  $K_1$  on the addendum of the FS tooth and the point  $K_2$  on the left tooth profile of the CS tooth, and the meshing backlash  $j_{out}$  on the engaging-out arc is defined as the circumferential distance between the left endpoint on the addendum of the FS tooth and the right tooth profile of another CS tooth [10]. Since the position of point  $K_1$  is close to that of point  $K_2$ , the linear distance between them is usually used to calculate  $j_{in}$  and  $j_{out}$  [11], [16]. Moreover, the midpoint on the addendum of the CS tooth is denoted by D. The tangent line of the addendum circle of the CS through point D is denoted by  $L_1$ , and its parallel line through point A is denoted by  $L_2$ . Since the FS tooth rotates in the meshing process, the meshing depth  $h$  is defined as the vertical distance between lines  $L_1$  and  $L_2$  [10]. In order to calculate  $j_{in}$ ,  $j_{out}$  and  $h$  of the HD, the positions of the FS and CS teeth in the meshing process should be obtained, which are determined by the deformation characteristics of the FS and affected by the contact relationship between the FS and CS teeth [14], [28].

**C. THEORETICAL MODELS OF THE MESHING PARAMETERS**

In existing theoretical methods, the elastic deformation of the FS is usually described by the planar deformation of the neutral line on the middle cross section of the tooth rim [10], [16], [28], [32]. As shown in Figure 2(b), the neutral line of the FS before and after deformation are denoted by the red circle and black ellipse, respectively.  $r_m$  is the radius of the undeformed neutral line of the FS,  $\theta$  is the rotation angle of the WG, and  $w_0$  is the maximum radial displacement of the FS, which can be expressed as [10]

$$w_0 = m \cdot (Z_G - Z_R)/2 \tag{1}$$

where  $m$  is the module of the HD,  $Z_R$  and  $Z_G$  are the teeth number of the FS and CS, respectively. Based on the theory of rings, the deformation of point  $P_F$  on the neutral line of the FS at  $\theta$  position ( $P_F \rightarrow P'_F$ ) can be described by the radial displacement  $w$ , circumferential displacement  $v$ , and rotation angle  $\varphi$  of the normal line ( $N_F \rightarrow N'_F$ ) [10], [22]

$$\begin{cases} w = w_0 \cdot \cos(2\theta) \\ v = -(w_0/2) \cdot \sin(2\theta) \\ \varphi = [3w_0/(2r_m)] \cdot \sin(2\theta). \end{cases} \tag{2}$$

Further, a kinematics model of the HD proposed by Ivanov [10] is used to calculate the positions of the FS and CS teeth in the meshing process, which is widely used up to now [14], [33], [36]. As shown in Fig. 2(c), a rectangular coordinate system  $Oxy$  is established on one tooth pair located at the minor axis of the WG. The  $y$ -axis is the symmetry axis of the tooth pair, and the origin  $O$  is the intersection point of the  $y$  axis and undeformed neutral line of the FS. The positions of the FS and CS teeth are described by the midpoints on their addendums and dedendums, whose coordinates are defined as A ( $x_{aR}, y_{aR}$ ), B ( $x_{fR}, y_{fR}$ ), C ( $x_{aG}, y_{aG}$ ) and D ( $x_{fG}, y_{fG}$ ). Based on the obtained deformation parameters of

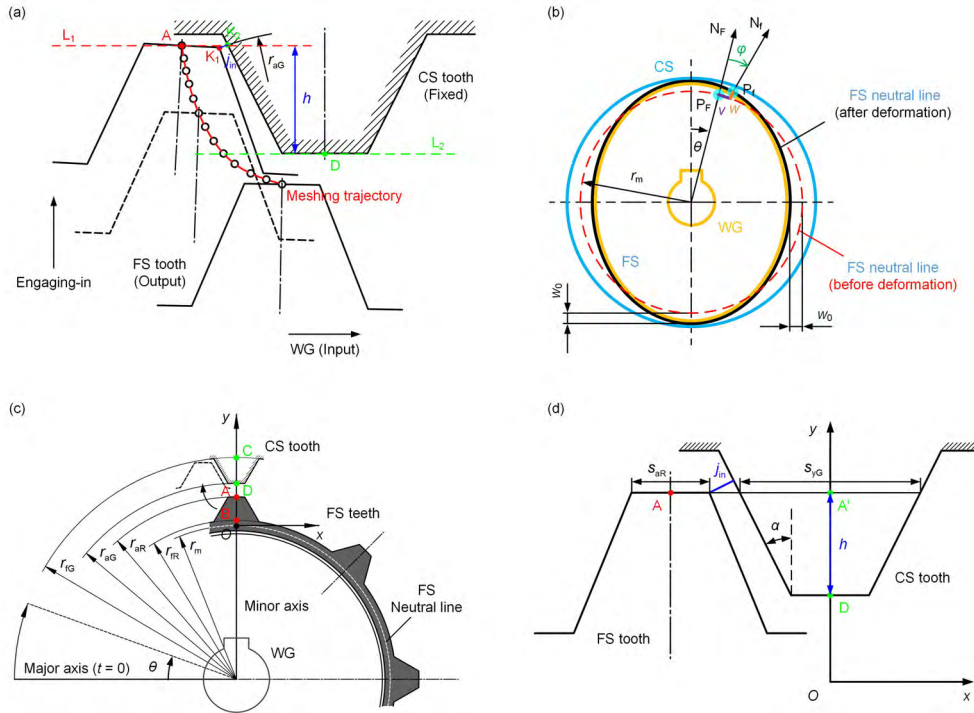


**FIGURE 2.** Parameters for characterizing the meshing performance of the HD and their corresponding theoretical models. (a) Relative motion of one meshed tooth pair in the engaging-in phase, and the definitions of the meshing backlash and depth; (b) theoretical model of the elastic deformation of the FS; (c) theoretical model for calculation of the positions of the FS and CS teeth in the meshing process; (d) theoretical model of the meshing backlash and depth.

the FS in (2), the coordinates of points A-D in the meshing process can be expressed as [10]

$$\begin{cases} x_{aR} = v + \varphi \cdot (r_{aR} - r_m) - (r_{aR} + w) \cdot (\theta/i_{GR}) \\ y_{aR} = (r_{aR} + w) \cdot \cos(\theta/i_{GR}) - r_m \\ x_{fR} = v + \varphi \cdot (r_{fR} - r_m) - (r_{fR} - w) \cdot (\theta/i_{GR}) \\ y_{fR} = (r_{fR} + w) \cdot \cos(\theta/i_{GR}) - r_m, \end{cases} \quad (3)$$

$$\begin{cases} x_{aG} = 0 \\ y_{aR} = r_{aG} - r_m \\ x_{fG} = 0 \\ y_{fG} = r_{fG} - r_m \end{cases} \quad (4)$$

where  $i_{GR}$  is the reduction ratio of the HD.  $r_{aR}$  and  $r_{fR}$  are the radii of the addendum and dedendum circles of the FS, respectively.  $r_{aG}$  and  $r_{fG}$  are the radii of the addendum and dedendum circles of the CS, respectively. Last, as shown in Fig. 2(d),  $j_{in}$ ,  $j_{out}$  and  $h$  of the HD at  $\theta$  position can be calculated by the obtained positions of the FS and CS teeth in (3)-(4) [10]

$$\begin{cases} j_{in} = [|x_{aR}| - (s_{aR} + s_{yG})/2] \cdot \cos \alpha \\ j_{out} = [(r_m + y_{aR}) \cdot 2\pi/Z_G - |x_{aR}| - (s_{aR} + s_{yG})/2] \\ \quad \cdot \cos \alpha \\ h = y_{aR} - y_{aG}, \end{cases} \quad (5)$$

where  $\alpha$  is the pressure angle of the HD,  $s_{aR}$  is the tooth thickness of the FS at the addendum circle, and  $s_{yG}$  is the tooth

thickness of the CS at the position of the addendum circle of the FS.  $s_{aR}$  and  $s_{yG}$  can be calculated by the modification coefficients of the FS  $x_R$  and CS  $x_G$ , respectively [10].

### III. PROPOSED METHOD

#### A. FRAMEWORK

The HD meshing performance analysis framework is composed of three phases, acquisition of the meshing images, tracking of the meshed teeth pairs, and calculation of the meshing parameters. A schematic diagram describing the procedure of developing the proposed meshing performance analysis framework is illustrated in Fig. 3. In the first phase, an optical measurement method based on the principle of periscope is proposed to acquire the meshing images of the HD at different driving speed and load torque. In the second phase, a position tracking algorithm based on image processing and pattern recognition is designed to obtain the positions of the FS and CS teeth in the meshing process. In the third phase, a mathematical model based on the geometric relationship between the FS and CS teeth is established to calculate the meshing backlash and depth of the HD. Each phase of the proposed framework will be discussed in detail in the following subsections.

#### B. ACQUISITION OF THE MESHING IMAGES

Since the gear engagement of the HD is realized through the elastic deformation of the FS, the meshing process of

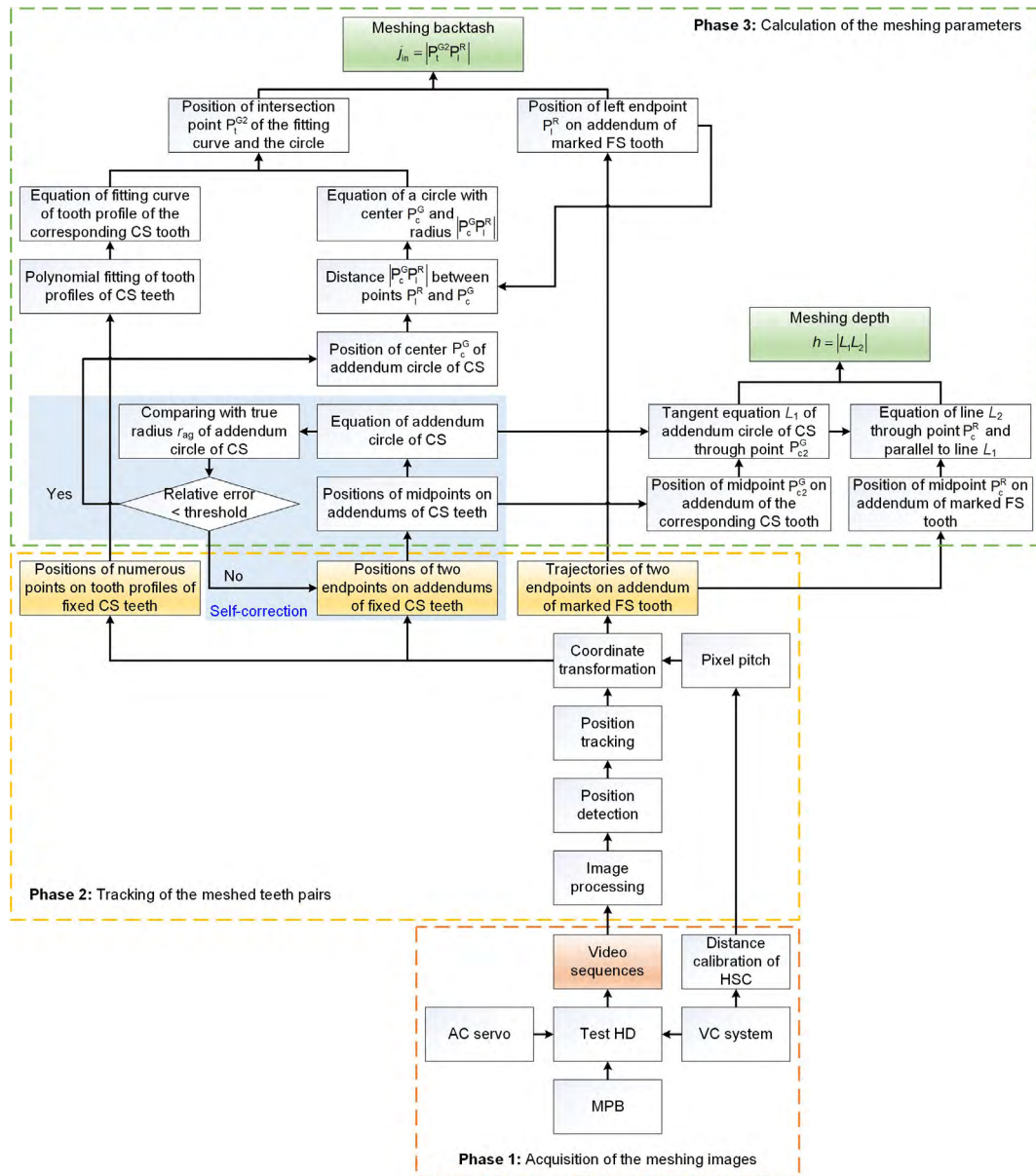
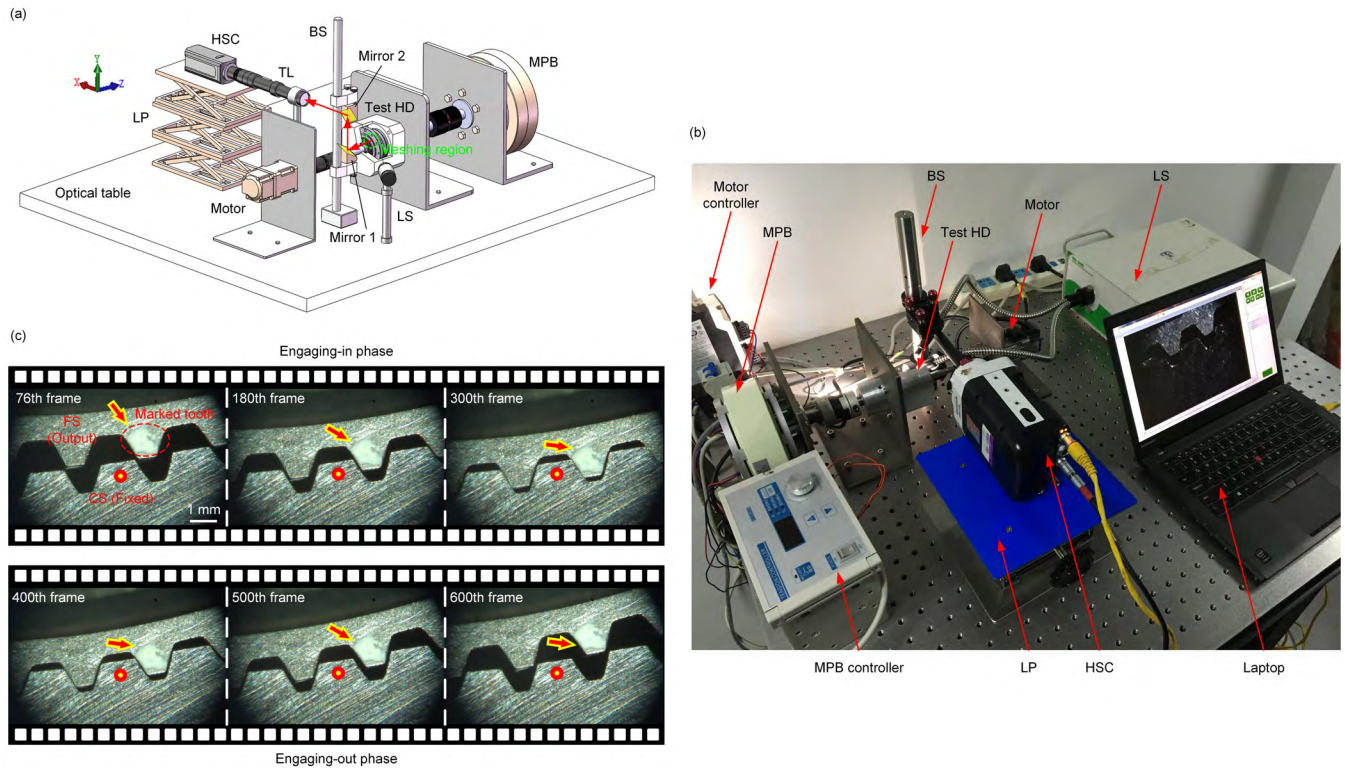


FIGURE 3. Schematic diagram of the HD meshing performance analysis framework.

the HD should be analyzed in the three-dimensional space in theory. However, for a normal HD with a cylindrical FS, the deflection the FS teeth along the rotating axis in the meshing process can be ignored due to its small value, which is about 0.08% of the diameter of the FS [16]. Thus, the meshing images of the HD are acquired by a two-dimensional HSC (M110, Phantom, USA) in this work. The key technique problem for measuring the meshing process is how to ensure the HD can work under various operating conditions. In existing measurement methods, the test HD was installed backwards through a transmission part and the HSC was directly put in front of the meshing region [14]. However, since the output side of the test HD was close to the motor, the loader cannot be installed any more. To solve this problem, an optical

measurement method for the meshing process of the test HD is proposed based on the principle of periscope, and the developed experimental apparatus is suitable for different driving, loading and lubrication conditions.

As shown in Fig. 4(a), the experimental apparatus contains a HD system and a video capture (VC) system. In the HD system, the motor (MSMD012G1U, Panasonic, Japan), test HD (XB1-40-50, CTKM, China) and magnetic powder brake (MPB, PB1.2, China) are sequentially connected through two couplings, and their center line is along the Z-axis. The motor and MPB are utilized to adjust the driving speed  $n_{in}$  and load torque  $T_{out}$  of the test HD, respectively. The test HD has an elliptical cam WG and involute tooth profile. The WG works as the input part and is linked with the motor



**FIGURE 4.** Acquisition of the meshing images of the HD under various operating conditions. (a) Schematic diagram of the proposed optical measurement method for the meshing process of the HD based on the principle of periscope; (b) The corresponding experimental apparatus; (c) Obtained video sequences of the meshing process of the test HD at  $n_{in} = 1$  r/min,  $T_{out} = 0$  N·m and  $s = 20$  fps.

shaft, the FS works as the output part and is linked with the MPB shaft, and the CS is fixed on the outer box. Furthermore, a third of the outer box of the test HD is removed through wire cutting to expose the meshing region, which is indicated by the green dotted circle. Obviously, the HSC cannot be directly put in front of the meshing region in this case. In the VC system, a beam steerers (BS) is installed in front of the meshing region, and two protected silver mirrors (GCC-10220, Daheng Optics, China) are mounted on the BS. The HSC is fixed on a lifting platform (LP), a telecentric lens (TL, WWL30-110CT, Coolens, China) is mounted on the HSC, and their center line is along the X-axis. A light source (LS, XD-300-250, China) is fixed beside the BS and obliquely irradiates on the meshing region to provide enough light for the HSC. In addition, the centers of the mirror 1 and mirror 2 are made towards the meshing region (The Z-axis) and the TL of the HSC (The X-axis), respectively. Moreover, the positions of the HSC and two mirrors can be adjusted by the LP and the mirror mounts of the BS, respectively. It can be seen that the light path denoted by the red arrow is changed from the negative direction of the Z-axis to the positive direction of the X-axis after twice reflections on the mirror 1 and mirror 2. Therefore, when the light intensity of the LS and the positions of the HSC as well as two mirrors are precisely adjusted, clear meshing images of the test HD can be captured by the HSC. In the experiments,  $n_{in}$  is changed from 1 r/min to

200 r/min because the HD used in the robots usually operates at ultra-low speed,  $T_{out}$  is changed from 0 N·m to 8 N·m since the rated output torque of the test HD is 10 N·m, and the test HD works under dry friction condition. The resolution of the HSC is  $1280 \times 800$ , and its frame rate  $s$  and exposure time are set according to the values of  $n_{in}$  and  $T_{out}$ . Three trials are performed under each working condition, and at least one complete meshing process of the test HD is recorded in each trial.

Figure 4(b) shows the obtained video sequences of the meshing process of the test HD when  $n_{in} = 1$  r/min,  $T_{out} = 0$  N·m, and  $s = 20$  fps (Frames per second). In each video frame, the fixed CS tooth is indicated by the point, and the corresponding FS tooth is indicated by the arrow. In order to improve the computational accuracy and efficiency of the designed position tracking algorithm that will be introduced in the next section, the FS tooth is marked with the white paint before the experiments, which is indicated by the red dotted ellipse. In addition, the meshing characteristics of the test HD are investigated only in the engaging-in, engagement and engaging-out phases because the disengagement phase is usually not considered in the meshing analysis of the HD [10]. It is shown that as the WG rotates clockwise, the FS teeth first engage with the CS teeth (From 76th frame to 300th frame), and then enter into the engagement phase (From 300th frame to 400th frame), and finally disengage with the CS teeth

(From 400th frame to 600th frame). In addition, the FS teeth change their positions and orientations in the meshing process. Since the deformation of the FS teeth is usually ignored [15], [16], the motion of the FS teeth in the meshing process can be viewed as the plane motion of rigid bodies.

### C. TRACKING OF THE MESHED TEETH PAIRS

The next step is to obtain the positions of the FS and CS teeth in the meshing process based on the acquired meshing images of the HD. Among existing object detection and tracking methods, the computational accuracy of the convolutional neural network (CNN) based method is much higher than that of the conventional template matching method [37]. However, CNN may not be a good choice for tracking the meshed teeth pairs of the HD. As shown in Fig. 4(b), the shapes of the FS and CS teeth are simple and regular, and the background of each video frame is nearly constant. Moreover, the HSC and TL in the experiments are fixed, and the motion of the FS teeth in the video sequences only contains the translation and rotation. Therefore, the template matching method used for tracking the FS teeth in the meshing process can achieve higher computational efficiency and simpler algorithm structure than the CNN based method. The fixed positions of the CS teeth in video sequences can be easily detected by common image processing algorithms. Fig. 5 shows the flowchart of the designed position tracking algorithm.

#### 1) POSITION DETECTION OF THE FIXED CS TEETH

To calculate the meshing parameters of the HD, positions of the tooth profiles and two endpoints on the addendums of the fixed CS teeth should be detected, which can be seen in Fig. 3. Since the positions of the fixed CS teeth in each video frame are same, the detection work is only performed in the first video frame and shown in the red region of Fig. 5. On the one hand, the positions of the two endpoints on the addendum of the CS tooth are obtained manually in the original image. On the other hand, the tooth profiles of the CS tooth are first extracted by the Canny algorithm [38] and then detected manually to obtain their positions. The detection results of the CS teeth are shown in Fig. 6, the cyan lines and yellow crosses denote the detected tooth profiles and endpoints on the addendums of the CS teeth, respectively.

#### 2) POSITION TRACKING OF THE OUTPUT FS TOOTH

The implementation of the position tracking of the marked FS tooth in the meshing process based on the template matching method is shown in the blue region of Fig. 5, and the major substeps include template generation, image processing, template matching, position detection and position tracking. In the substep of template matching, the marked FS tooth in the first video frame is cut by a rectangle to generate the template image. Moreover, the left and right endpoints on the addendum of the marked FS tooth are set as the tracked points, and their positions  $(X_0, Y_0)$  in the template image are recorded manually for the substep of position detection. After that, all the video frames and the template image are

converted to the gray images, and the normalization, erosion, dilation and median filtering are performed sequentially to improve the quality of the gray images [39]. The substep of template matching is operated based on the SURF (Speeded up robust features) algorithm [40]. The positions and descriptor vectors of the feature points of the template image and each video frame are obtained. These feature points are matched according to the distance between their descriptor vectors, and at least two groups of the feature points should be matched successfully for the substep of position detection. Further, the positions  $(X_a, Y_a)$  of the two tracked points in each video frame are calculated by their positions  $(X_0, Y_0)$  in the template image which have been obtained in the substep of template generating using the similarity transformation [41], and the coordinate transformation matrix  $M_i$  is estimated by the positions of the above matched feature points based on the MSAC (M-estimator sample consensus) algorithm [42]. In the substep of position tracking, to verify the effectiveness of the calculated positions of the tracked point, the distance  $D_a$  between the tracked point in the current  $(X_a, Y_a)$  and previous  $(X_{a-1}, Y_{a-1})$  video frames is calculated to compare with a pre-set threshold  $D_{\text{threshold}}$ . Last, the positions of the two tracked points in all video frames are obtained. As shown in Fig. 6, the blue and red curves denote the tracked motion trajectories of the left and right endpoints on the addendum of the marked FS tooth in the meshing process, respectively.

#### 3) TRANSFORMATION OF THE COORDINATE SYSTEMS

The calculated position data of the meshed teeth pairs in the meshing process of the HD are further transformed from the pixel coordinate system (Unit: pixel) into the physical coordinate system (Unit: mm) through calibrating the HSC. As shown in Fig. 7(a),  $(X, Y)$  and  $(x, y)$  represent the coordinates of one point on the FS tooth defined in the pixel and physical coordinate systems, respectively. The transformation relationship between  $(X, Y)$  and  $(x, y)$  can be expressed as

$$(x, y) = \mu \cdot (X, Y), \quad (6)$$

where  $\mu$  is the pixel pitch (Unit: mm/pixel), and it is obtained through a normal distance calibration experiment of the HSC. The experimental result is shown in Fig. 7(b), a line segment on the steel rule is selected and its length is defined as  $L$ . Here,  $L$  is equal to 3 mm. Further, the left and right endpoints of the line segment are picked, and their coordinates are denoted by  $(X_L, Y_L)$  and  $(X_R, Y_R)$ , respectively. Since  $Y_L$  is equal to  $Y_R$ ,  $\mu$  can be calculated as follows

$$\mu = \frac{L}{X_R - X_L}. \quad (7)$$

The above calculation is repeated twenty times, and the arithmetic mean of the results is used as the final value of  $\mu$ .

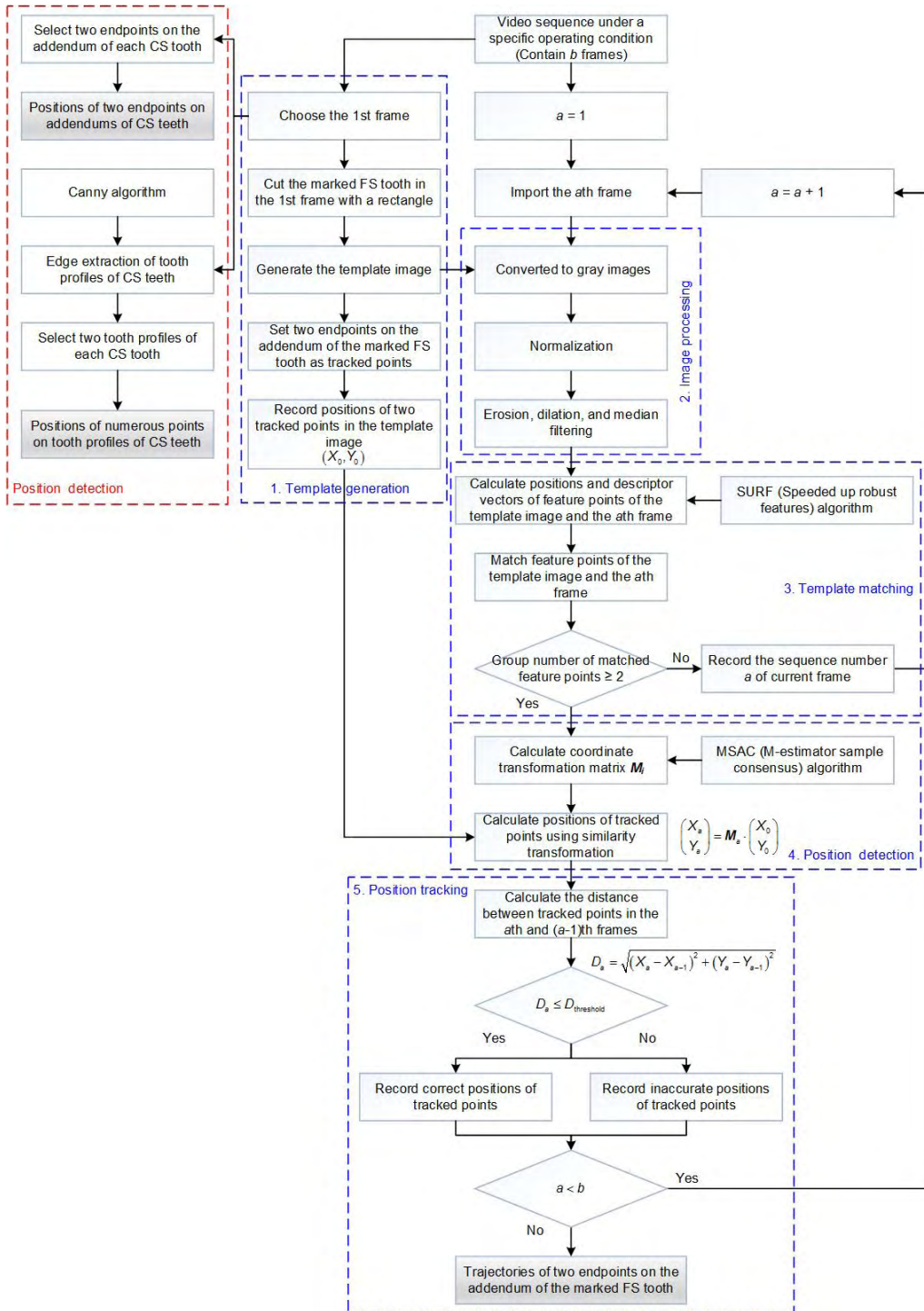


FIGURE 5. Flowchart of the designed position tracking algorithm for the meshed teeth pairs of the HD.

**D. CALCULATION OF THE MESHING PARAMETERS**

In the above section, for the meshing process of the HD under various operating conditions, the positions of the tooth profiles and two endpoints on the addendums of the fixed CS teeth are detected, and the trajectories of the two endpoints on the addendum of the marked FS tooth are tracked. Based on

the acquired position data of the FS and CS teeth in the meshing process, a mathematical model based on the geometric relationship between the FS and CS teeth is established to calculate  $j_{in}$ ,  $j_{out}$  and  $h$  of the HD. As shown in Fig. 8, three fixed CS teeth, from the left to right, are defined as  $G_1$ ,  $G_2$ , and  $G_3$ , respectively. The left and right endpoints on the



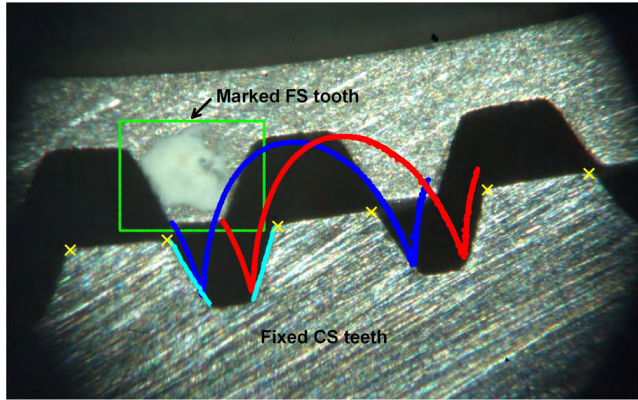


FIGURE 6. Tracking result of the meshed teeth pairs of the HD in the meshing process.

addendum of tooth  $G_i (i = 1, 2, 3)$  are defined as  $P_{li}^G(x_{li}^G, y_{li}^G)$  and  $P_{ri}^G(x_{ri}^G, y_{ri}^G)$ , respectively. A series of points on the right tooth profile of tooth  $G_2$  are defined as  $P_{ij}^G(x_{ij}^G, y_{ij}^G) (j = 1, 2, \dots, n)$ , and  $n$  is the number of these points. Moreover, the marked FS tooth is defined as  $R$ , and the left and right end-points on the addendum of tooth  $R$  are defined as  $P_1^R(x_1^R, y_1^R)$  and  $P_r^R(x_r^R, y_r^R)$ , respectively. As mention in Section 3.2, the engaging-in, engagement and engaging-out phases are investigated in this work, and the total computing time is nearly half of the meshing period of the HD. As shown in Fig. 4(b), the initial time  $t_{\text{initial}}$  corresponds to the 76th frame where the addendums of teeth  $R$  and  $G_2$  are collinear, and the terminal time  $t_{\text{terminal}}$  corresponds to the 600th frame where the addendums of teeth  $R$  and  $G_3$  are collinear. Time  $t_a$  corresponding to the  $a$ th frame can be expressed as

$$t_a = \frac{1}{s} \cdot a \quad (a = 1, 2, \dots, b). \quad (8)$$

As mentioned in Section 2.1, since the double-wave WG is used in the test HD and  $Z_R$  is two fewer than  $Z_G$ , the meshing period of the HD is half of the rotating period of the WG, and the total computing time varies with  $n_{\text{in}}$ . To solve this problem,  $\theta$  is used to quantify the meshing process of the HD, and  $\theta_a$  at  $t_a$  can be expressed as

$$\theta_a = 2\pi \cdot \frac{n_{\text{in}}}{60} \cdot t_a \cdot \frac{180}{\pi}. \quad (9)$$

Further, the total rotation angle  $\theta_{\text{total}}$  of the WG corresponding to the total computing time can be calculated by  $\theta_{\text{initial}}$  at  $t_{\text{initial}}$  and  $\theta_{\text{terminal}}$  at  $t_{\text{terminal}}$

$$\theta_{\text{total}} = \theta_{\text{terminal}} - \theta_{\text{initial}}. \quad (10)$$

The calculation process has been illustrated in Fig. 3, and specific steps are presented as follows.

### 1) CALCULATION OF THE MESHING BACKLASH

First, the midpoint on the addendum of each CS tooth is defined as  $P_{ci}^G(x_{ci}^G, y_{ci}^G)$ , and its coordinate can be calculated

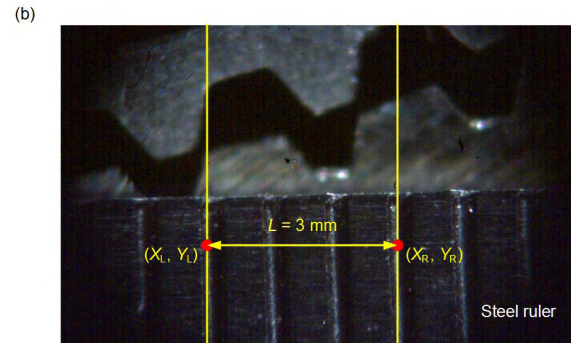
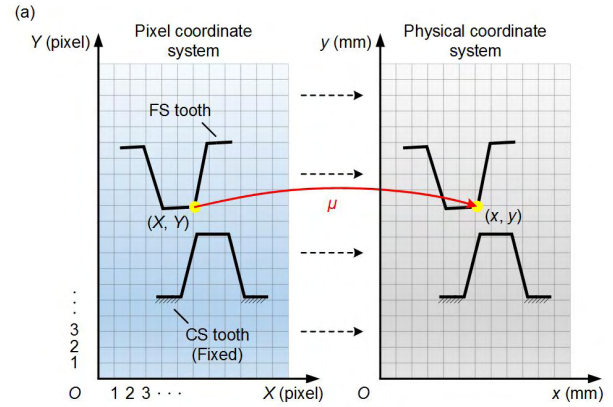


FIGURE 7. Transformation of the coordinate systems through calibrating of the HSC. (a) Coordinates of the meshed teeth pairs of the HD defined in pixel and physical coordinate systems, and the transformation relationship between them; (b) Experiment result of the distance calibration of the HSC.

by the coordinates of points  $P_{li}^G$  and  $P_{ri}^G$

$$\begin{cases} x_{ci}^G = \frac{x_{li}^G + x_{ri}^G}{2} \\ y_{ci}^G = \frac{y_{li}^G + y_{ri}^G}{2} \end{cases} \quad (i = 1, 2, 3). \quad (11)$$

Next, the center of the addendum circle of the CS is defined as  $P_c^G(x_c^G, y_c^G)$ , and the distance between points  $P_{ci}^G$  and  $P_c^G$  is defined as  $s_i$ , which can be expressed as

$$s_i = \sqrt{(x_{ci}^G - x_c^G)^2 + (y_{ci}^G - y_c^G)^2} \quad (i = 1, 2, 3). \quad (12)$$

Since  $s_1, s_2,$  and  $s_3$  are all the radii of the addendum circle of the CS, they should meet the following relationship

$$s_1 = s_2 = s_3. \quad (13)$$

Then, the coordinate of point  $P_c^G$  can be calculated by substituting (12) into (13). In order to ensure the accuracy of the calculated  $x_c^G$  and  $y_c^G$  for the subsequent calculation, the calculated  $s_i$  is compared with the true value of  $r_{aG}$  obtained from the manufacturer. If the relative error between  $s_i$  and  $r_{aG}$  is greater than a preset threshold, points  $P_{li}^G$  and  $P_{ri}^G$  will be detected again in Section 3.3.1. This self-correction process is shown in the blue region of Fig. 3. The right tooth profile of tooth  $G_2$  is fitted by a 5th order polynomial, which can be

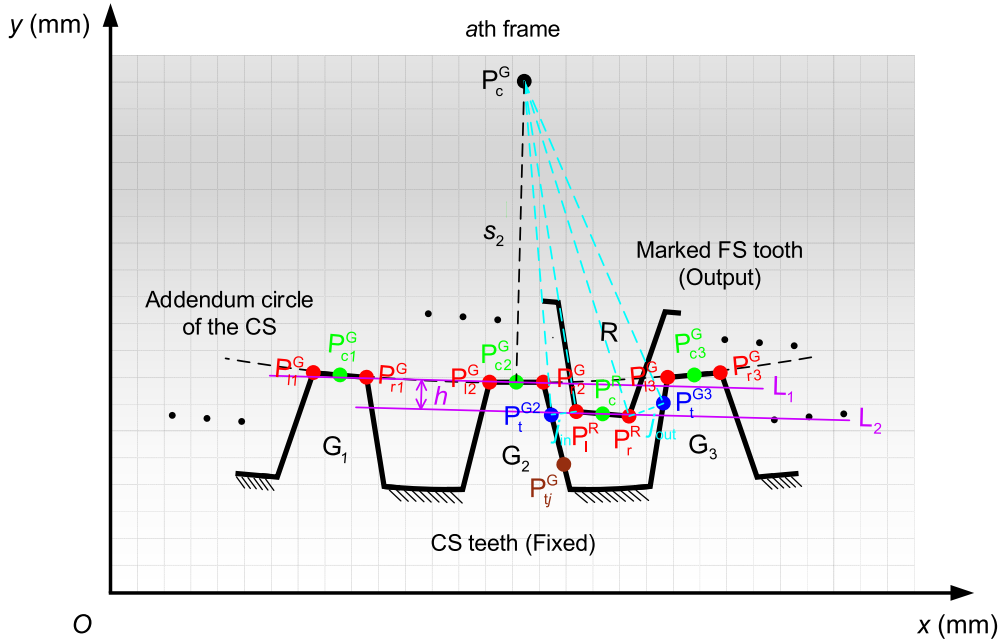


FIGURE 8. Mathematical model for calculation of the meshing parameters of the HD.

expressed as

$$y = a_0 + a_1x + a_2x^2 + a_3x^3 + a_4x^4 + a_5x^5, \quad (14)$$

where  $a_0, a_1, a_2, a_3, a_4,$  and  $a_5$  are the coefficients, and they can be calculated by the coordinate of point  $P_{ij}^G$  based on the least square method. Similarly, the fitting error is controlled to be close to zero.

Further, the point  $P_c^G$  is defined as the center of a circle whose radius is equal to the distance between points  $P_1^R$  and  $P_c^G$ . The intersection point of the circle and the right tooth profile of tooth  $G_2$  is defined as  $P_t^{G2}(x_t^{G2}, y_t^{G2})$ , and its coordinate can be calculated by the following equations

$$\begin{cases} (x_t^{G2} - x_c^G)^2 + (y_t^{G2} - y_c^G)^2 = (x_1^R - x_c^G)^2 \\ + (y_1^R - y_c^G)^2 \\ y_t^{G2} = a_0 + a_1 \cdot x_t^{G2} + a_2 \cdot (x_t^{G2})^2 + a_3 \cdot (x_t^{G2})^3 \\ + a_4 \cdot (x_t^{G2})^4 + a_5 \cdot (x_t^{G2})^5. \end{cases} \quad (15)$$

Thus,  $j_{in}$  can be expressed as the distance between points  $P_t^{G2}$  and  $P_1^R$

$$j_{in} = \sqrt{(x_t^{G2} - x_1^R)^2 + (y_t^{G2} - y_1^R)^2}. \quad (16)$$

Likewise, the left tooth profile of tooth  $G_3$  is fitted by a 5th order polynomial. The point  $P_c^G$  is defined as the center of a circle whose radius is equal to the distance between points  $P_1^R$  and  $P_c^G$ . The intersection point of the circle and the left tooth profile of tooth  $G_3$  is defined as  $P_t^{G3}(x_t^{G3}, y_t^{G3})$ , and  $j_{out}$  can be expressed as

$$j_{out} = \sqrt{(x_t^{G3} - x_1^R)^2 + (y_t^{G3} - y_1^R)^2}. \quad (17)$$

Last, the variations of  $j_{in}$  and  $j_{out}$  with  $\theta$  in the engaging-in, engagement and engaging-out phases of the HD can

be obtained, and their minima are defined as  $\min(j_{in})$  and  $\min(j_{out})$ , respectively.

## 2) CALCULATION OF THE MESHING DEPTH

First, the slope  $k$  of the line  $P_{c2}^G P_c^G$  can be expressed as

$$k = \frac{y_{c2}^G - y_c^G}{x_{c2}^G - x_c^G}. \quad (18)$$

The tangent line of the addendum circle of the CS through point  $P_{c2}^G$  is defined as  $L_1$ . Since line  $L_1$  is perpendicular to line  $P_{c2}^G P_c^G$ , the equation of line  $L_1$  can be expressed as

$$k(y - y_{c2}^G) + (x - x_{c2}^G) = 0. \quad (19)$$

Next, the midpoint on the addendum of tooth R is defined as  $P_c^R(x_c^R, y_c^R)$ , and its coordinate can be expressed as

$$\begin{cases} x_c^R = \frac{x_1^R + x_r^R}{2} \\ y_c^R = \frac{y_1^R + y_r^R}{2}. \end{cases} \quad (20)$$

Then, the parallel line of line  $L_1$  through point  $P_c^R$  is defined as line  $L_2$ , and its equation can be expressed as

$$k(y - y_c^R) + (x - x_c^R) = 0. \quad (21)$$

Further,  $h$  can be expressed as the vertical distance between lines  $L_1$  and  $L_2$

$$h = \frac{k(y_c^R - y_{c2}^G) + (x_c^R - x_{c2}^G)}{\sqrt{k^2 + 1}}. \quad (22)$$

Last, the variation of  $h$  with  $\theta$  in the engaging-in, engagement and engaging-out phases of the HD can be obtained, and its maximum is defined as  $\max(h)$ .

## E. UNCERTAINTY ANALYSIS OF THE CALCULATED MESHING PARAMETERS

The combined standard uncertainty (CSU) is used to evaluate the accuracies of the calculated  $j_{in}$ ,  $j_{out}$  and  $h$  of the HD [43]. According to (16),  $j_{in}$  is calculated by the coordinates of points  $P_1^R$  and  $P_t^{G2}$ . The coordinate of point  $P_1^R$  is measured directly, whereas the coordinate of point  $P_t^{G2}$  is calculated by the equation of the fitting curve of the right tooth profile of tooth  $G_2$  and the coordinates of points  $P_1^R$  and  $P_c^G$ . Furthermore, the equation of the fitting curve is calculated by the measured coordinate of point  $P_{ij}^G$ , and the coordinate of point  $P_c^G$  is calculated by the measured coordinates of points  $P_{li}^G$  and  $P_{ri}^G$ . Since the CS is fixed in the meshing process, its tooth profiles can be exactly extracted by the Canny algorithm, and the self-correction process can ensure the high precision of the detected endpoints on the addendums. Therefore, the uncertainties of the coordinates of points  $P_{ij}^G$ ,  $P_{li}^G$  and  $P_{ri}^G$  can be ignored, and the position accuracy of point  $P_t^{G2}$  only depends on that of point  $P_1^R$ . In this work, to simplify the calculation, it is assumed that the uncertainties of  $x_1^R$ ,  $y_1^R$ ,  $x_t^{G2}$  and  $y_t^{G2}$  are independent of each other, and the CSU of  $j_{in}$  can be expressed as [44]

$$u_c(j_{in}) = \sqrt{\left(\frac{\partial j_{in}}{\partial x_t^{G2}}\right)^2 u^2(x_t^{G2}) + \left(\frac{\partial j_{in}}{\partial x_1^R}\right)^2 u^2(x_1^R) + \left(\frac{\partial j_{in}}{\partial y_t^{G2}}\right)^2 u^2(y_t^{G2}) + \left(\frac{\partial j_{in}}{\partial y_1^R}\right)^2 u^2(y_1^R)}, \quad (23)$$

where  $u(x_1^R)$ ,  $u(y_1^R)$ ,  $u(x_t^{G2})$  and  $u(y_t^{G2})$  are the type A standard uncertainties of  $x_1^R$ ,  $y_1^R$ ,  $x_t^{G2}$  and  $y_t^{G2}$ , respectively. The CSU of  $j_{out}$  can be obtained in the same way, since its value is close to that of  $u_c(j_{in})$ , the calculation of the CSU of  $j_{out}$  is not performed in this work.

Similarly, according to (22),  $h$  is calculated by  $k$  and the coordinates of points  $P_c^R$  and  $P_{c2}^G$ . The coordinate of point  $P_c^R$  is calculated by the measured coordinates of points  $P_1^R$  and  $P_r^R$ , whereas  $k$  is calculated by the coordinates of points  $P_c^G$  and  $P_{c2}^G$ . Based on the above assumption, since the coordinates of points  $P_c^G$  and  $P_{c2}^G$  are calculated by the measured coordinates of points  $P_{li}^G$  and  $P_{ri}^G$ , the uncertainties of  $k$ ,  $x_{c2}^G$  and  $y_{c2}^G$  can be ignored, and the CSU of  $h$  can be expressed as [44]

$$u_c(h) = \sqrt{\left(\frac{\partial h}{\partial y_c^R}\right)^2 u^2(y_c^R) + \left(\frac{\partial h}{\partial x_c^R}\right)^2 u^2(x_c^R)}, \quad (24)$$

where  $u(x_c^R)$  and  $u(y_c^R)$  are the type A standard uncertainties of  $x_c^R$  and  $y_c^R$ , respectively.

Since three trials are performed under each operating condition in the experiments, the value of each coordinate can be estimated by the arithmetic mean of the three measured

values, which can be expressed as

$$z = \bar{z} = \frac{\sum_{e=1}^3 z_e}{3} \quad \left(z = x_1^R, y_1^R, x_t^{G2}, y_t^{G2}, x_c^R, y_c^R\right), \quad (25)$$

where  $z_e$  and  $\bar{z}$  denote the  $e$ th measured value and the arithmetic mean of  $z$ , respectively. Then, the type A standard uncertainty  $u(z)$  of  $z$  can be given by its experimental standard deviation [45]

$$u(z) = \sqrt{\frac{\sum_{e=1}^3 (z_e - \bar{z})^2}{3 \times 2}} \quad \left(z = x_1^R, y_1^R, x_t^{G2}, y_t^{G2}, x_c^R, y_c^R\right). \quad (26)$$

Substituting (25) and (26) into (23) and (24),  $u_c(j_{in})$  and  $u_c(h)$  at different  $\theta$  can be obtained. Further, the ratio  $r_{-u_c}(q)$  ( $q = j_{in}, j_{out}, h$ ) of the average  $u_c(q)$  to the average  $q$  in the meshing process are calculated to evaluate the accuracies of the calculated meshing parameters of the HD at different  $n_{in}$  and  $T_{out}$ , which can be expressed as

$$r_{-u_c}(q) = \frac{\text{mean}(u_c(q))}{\text{mean}(q)} \quad (q = j_{in}, j_{out}, h). \quad (27)$$

## IV. PERFORMANCE EVALUATION

### A. COMPUTATIONAL ACCURACY

The computational accuracy of the proposed method is evaluated based on the results of the uncertainty analysis. As shown in Fig. 9(a) and (b),  $u_c(j_{in})$  and  $u_c(h)$  nearly keeps constant in the meshing process and their values are little affected by  $n_{in}$ , which indicates that our method are robust for different operating conditions. The larger fluctuation of  $u_c(j_{in})$  at 200 r/min and  $u_c(h)$  at 10 r/min are mainly caused by the lower quality of the acquired meshing images of the HD under those working conditions. Moreover, Fig. 9(c) shows that  $r_{-u_c}(j_{in})$  of and  $r_{-u_c}(h)$  are very small at different  $n_{in}$ , and their arithmetic means are around 0.038% and 0.015%, respectively.  $r_{-u_c}(j_{in})$  is approximately twice of  $r_{-u_c}(h)$  at different  $n_{in}$  because the number of the uncertainty components of  $u_c(j_{in})$  is double that of  $u_c(h)$ , which can be seen in (19) and (20). Although the uncertainties of the coordinates of points  $P_{ij}^G$ ,  $P_{li}^G$  and  $P_{ri}^G$ , and the correlation between the coordinates of points  $P_t^{G2}$  and  $P_1^R$  are ignored in  $u_c(j_{in})$  and  $u_c(h)$ , it should be noticed that the positions of the FS and CS teeth in the meshing process are measured only three times in this work, and the uncertainties of the measured coordinates can be significantly reduced by performing more repeated measurements [44]. In addition, utilizing a HSC with higher resolution and a LS with higher illumination intensity can also decrease the uncertainties of the measured coordinates [43], and  $r_{-u_c}(j_{in})$  of and  $r_{-u_c}(h)$  can be kept near zero. The above results are discussed under no-load condition. Actually, the calculated  $u_c(j_{in})$  and  $u_c(h)$  under loading condition have the same characteristics, and a detailed illustration of them is not covered.

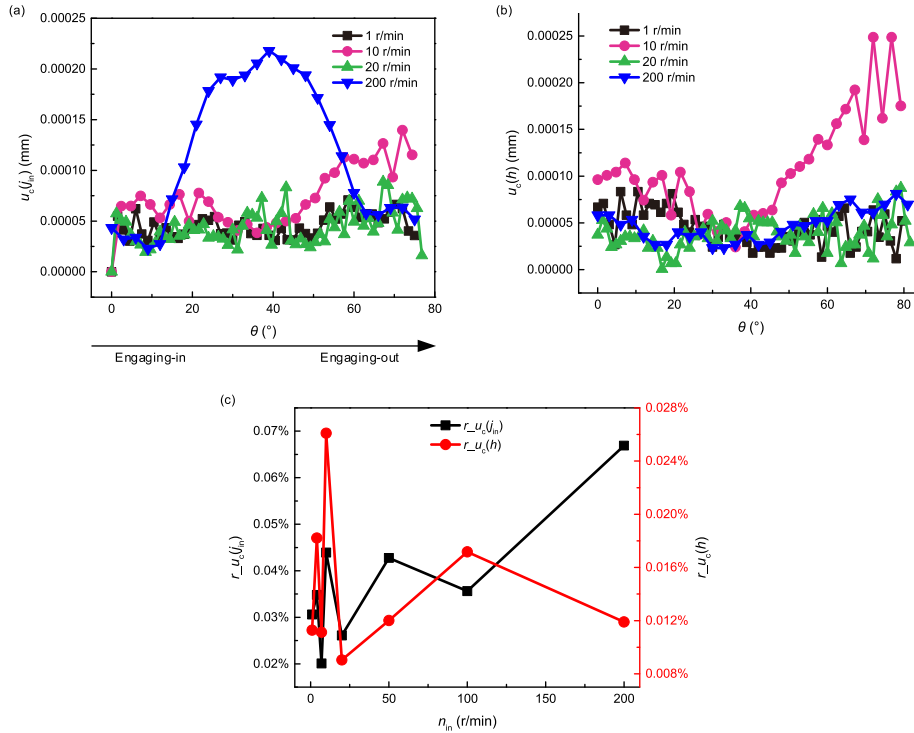


**FIGURE 9.** Results of the uncertainty analysis of the calculated meshing parameters of the HD. (a) and (b) Variations of  $u_c(j_{in})$  and  $u_c(h)$  with  $\theta$  at different  $n_{in}$ ; (c) Variation of  $r_{uc}(j_{in})$  and  $r_{uc}(h)$  with  $n_{in}$ .

**B. COMPUTATIONAL EFFICIENCY**

As shown in Fig. 3 and 5, the post-processing of the proposed method includes the tracking of the meshed teeth pairs and calculation of the meshing parameters. The running time of the post-processing is mainly consumed by tracking of the FS teeth and calculation of the meshing parameters. However, the time required to track the FS teeth is much greater than that required to calculate the meshing parameters, especially when the quantity of the acquired meshing images of the HD is large. Therefore, the processing speed of the designed position tracking algorithm for the FS teeth is used to evaluate the computational efficiency of our method. When run on a laptop with 2.6GHz CPU and 12GB RAM using MATLAB R2014a, the proposed method, on the average, takes 1.59 seconds per video frame for the position tracking of the FS teeth.

**C. SCOPE OF APPLICATION**

The developed experimental apparatus shown in Fig. 4(a) can be used to investigate the meshing performance of the HD under different driving, loading and lubrication conditions. In this work, the HD works under dry friction condition, and the effects of the driving speed and load torque on the meshing performance of HD are examined, which will be discussed in the following section. As we know, in the industrial and space robots, the grease and solid lubricants are usually used for the HD [46], [47]. Since the shape and color of the lubricants are different from the FS and CS teeth, designing an improved position tracking algorithm to

effectively classify the teeth and lubricants in the meshing images of the HD will be the focus of our future work.

**V. COMPARISON OF THE EXPERIMENTAL AND THEORETICAL RESULTS**

To further demonstrate the effectiveness and advantages of the proposed method, our results are compared with the theoretical results. Besides, the effects of  $n_{in}$  and  $T_{out}$  on the meshing performance of the HD are revealed, and the deficiencies of the theoretical model are discussed. The parameters of the test HD used for simulation of the theoretical model are given in Table 1, and the main calculation process can refer to Section 2.3. Since the meshing period of the HD is half of the rotating period of the WG, and the meshing performance of the HD are only investigated in the engaging-in, engagement and engaging-in phases,  $\theta_{total}$  is set to  $90^\circ$  in each simulation. In addition, the interval of  $\theta$  and the value of  $n_{in}$  set in the simulation are same as that set in the proposed method.

The comparison results are shown in Fig. 10, and each figure is plotted as a stack curve. The upper, middle and bottom panels describe the variations of the calculated  $j_{in}$ ,  $j_{out}$  and  $h$  by the proposed and theoretical methods with  $\theta$ , respectively. It is shown that the variation tendencies of  $j_{in}$ ,  $j_{out}$  and  $h$  obtained by two methods are nearly consistent, which confirms the effectiveness of the proposed method. Moreover, it should be noticed that the maximum of  $\theta$  in the measured  $h - \theta$  curve is equal to  $\theta_{total}$ , which can refer to Section 3.4.2. However, it is likely that (16) and (17) have

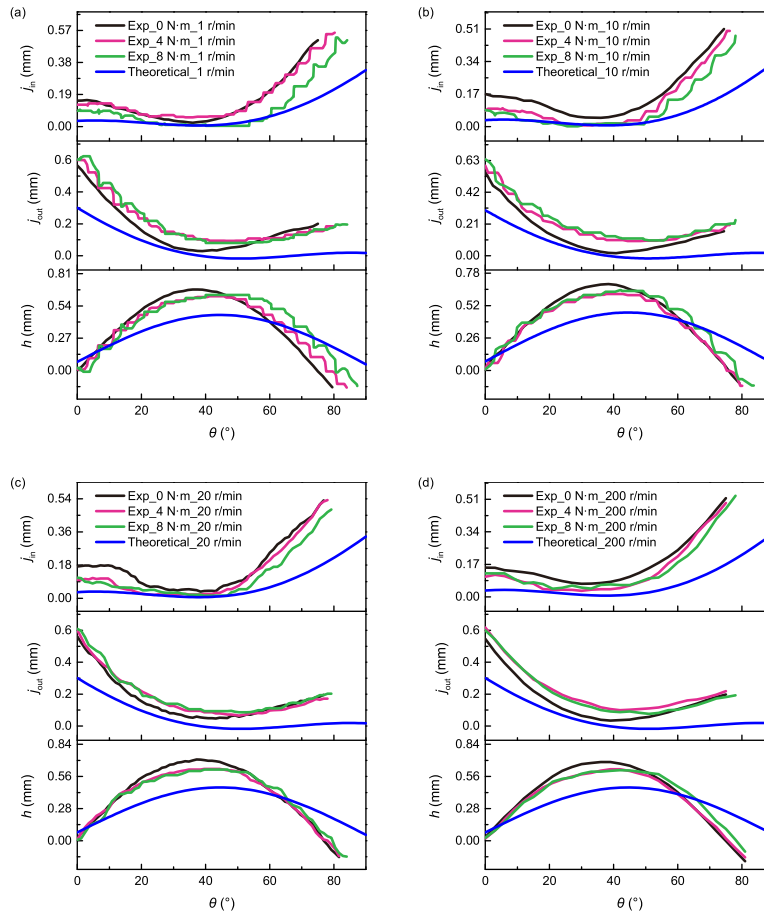


**FIGURE 10.** Comparison of the experimental and theoretical results at different  $n_{in}$ , and  $T_{out} = 0$  N·m, 4 N·m and 8 N·m in the experimental results. (a)  $n_{in} = 1$  r/min; (b)  $n_{in} = 10$  r/min; (c)  $n_{in} = 20$  r/min; (d)  $n_{in} = 200$  r/min.

**TABLE 1.** Parameters of the test HD used for simulation of the theoretical model.

Symbol	Quantity	Value
$m$	Module	0.4 mm
$Z_R$	Teeth number of the FS	100
$Z_G$	Teeth number of the CS	102
$d_{aR}$	Diameter of the addendum circle of the FS	42.050 mm
$d_{aG}$	Diameter of the addendum circle of the CS	41.900 mm
$d_{fR}$	Diameter of the dedendum circle of the FS	40.900 mm
$d_{fG}$	Diameter of the dedendum circle of the CS	43.060 mm
$d_m$	Diameter of the undeformed FS neutral line	40.350 mm
$x_R$	Modification coefficient of the FS	2.470
$x_G$	Modification coefficient of the CS	2.420
$\alpha$	Pressure angle	20

no solutions in the initial stage of the engaging-in phase and the final stage of the engaging-out phase, and thus the maximum of  $\theta$  in the measured  $j_{in} - \theta$  or  $j_{out} - \theta$  curve is always smaller than that in the measured  $h - \theta$  curve. The differences between the experimental and theoretical results are concluded as follows.

(a) The measured  $\theta_{total}$  is always smaller than  $90^\circ$ , and it is affected by  $n_{in}$  and  $T_{out}$ .

(b) The theoretical  $j_{in} - \theta$ ,  $j_{out} - \theta$  and  $h - \theta$  curves at any  $n_{in}$  are smooth, whereas the shapes of the measured  $j_{in} - \theta$ ,  $j_{out} - \theta$  and  $h - \theta$  curves are affected by  $n_{in}$  and  $T_{out}$ . At  $T_{out} = 0$  N·m, the measured  $j_{in} - \theta$ ,  $j_{out} - \theta$  and  $h - \theta$  curves at any  $n_{in}$  are smooth. However, at  $T_{out} = 4$  N·m, the “stick-slip phenomenon” exists in the measured  $j_{in} - \theta$ ,  $j_{out} - \theta$  and  $h - \theta$  curves when  $n_{in} \leq 10$  r/min, whereas these curves are similar to that at  $T_{out} = 0$  N·m when  $n_{in} > 10$  r/min. The results at  $T_{out} = 8$  N·m are consistent with that at  $T_{out} = 4$  N·m, except the critical speed of the “stick-slip phenomenon” increases to 20 r/min.

(c) In the theoretical results,  $\min(j_{in})$ ,  $\min(j_{out})$  and  $\max(h)$  are nearly constant. However, our results show that the  $\min(j_{in})$ ,  $\min(j_{out})$  and  $\max(h)$  are always greater than the theoretical ones, and they are affected by  $n_{in}$  and  $T_{out}$ .

### A. ATTENUATION AND VARIABILITY OF THE TOTAL ROTATION ANGLE

Our results reveal the attenuation and variability of  $\theta_{total}$  under actual operating conditions, and the specific effects of

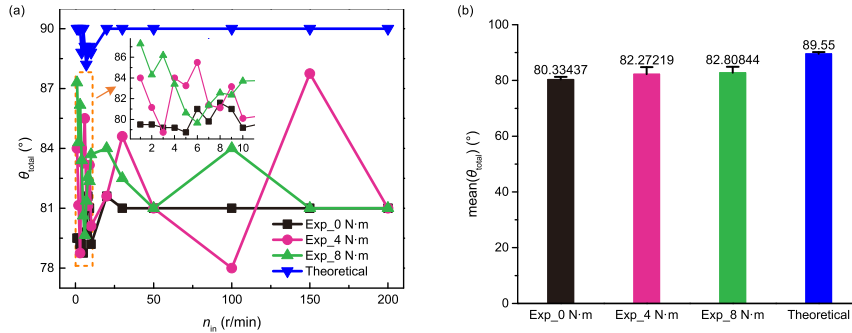


**FIGURE 11. Effects of  $n_{in}$  and  $T_{out}$  on  $\theta_{total}$ . (a) Comparison of the theoretical and measured  $\theta_{total}$  at different  $n_{in}$  and  $T_{out}$ ; (b) Comparison of the arithmetic means of the theoretical and measured  $\theta_{total}$  at different  $T_{out}$ .**

$n_{in}$  and  $T_{out}$  on  $\theta_{total}$  are further discussed here. Fig. 11(a) shows the comparison of the theoretical and measured  $\theta_{total}$  at different  $n_{in}$  and  $T_{out}$ . Because the interval of  $\theta$  set in the simulation at different  $n_{in}$  are not consistent and their values are not small enough, it can be seen that the theoretical  $\theta_{total}$  is slightly smaller than  $90^\circ$  at low speed. Furthermore, since the measured  $\theta_{total}$  fluctuates with  $n_{in}$  at any  $T_{out}$ , its arithmetic mean and standard deviation are calculated and shown in Fig. 11(b), and the standard deviation is denoted by the error bar to describe the fluctuation degree of  $\theta_{total}$  with  $n_{in}$ . The results show that at  $T_{out} = 0$  N·m,  $\theta_{total}$  nearly keeps constant as  $n_{in}$  increases, and only a slight fluctuation can be seen at low speed, which is similar to that found in the theoretical results. However, the large fluctuation can be seen in the measured  $\theta_{total} - n_{in}$  curves at  $T_{out} = 4$  N·m and 8 N·m. Moreover, the average  $\theta_{total}$  under loading condition is greater than that under no-load condition, which can also be seen in the measured  $h - \theta$  curves in Fig. 10.

Based on above analyses, it can be concluded that the disengagement phase actually accounts for more than half of the meshing period of the HD, and the theoretical model can roughly predict the variation of  $\theta_{total}$  with  $n_{in}$  under no-load condition when considering the attenuation of  $\theta_{total}$ . For the test HD used in this work, the attenuation of  $\theta_{total}$  is about  $10^\circ$ , and it may vary with the type and size of the HD. In addition,  $\theta_{total}$  fluctuates dramatically with  $n_{in}$  under loading condition, and its value is larger than that under no-load condition. The increase of  $\theta_{total}$  under loading condition can be explained by the increase of the contact ratio. Previous researchers have pointed out that the number of the teeth pairs of the HD mating simultaneously under no-load condition is smaller than that under loading condition [10], [16], [48], and the increase of the contact ratio means a raise in actual meshing time which corresponds to  $\theta_{total}$  in this work.

**B. ABNORMAL VARIATIONS OF THE BACKLASH AND DEPTH WITH THE ROTATION ANGLE**

The comparison results show that the measured  $j_{in} - \theta$ ,  $j_{out} - \theta$  and  $h - \theta$  curves under no-load condition and the theoretical ones are both smooth at any  $n_{in}$ , whereas the “stick-slip

phenomenon” exists in the measured  $j_{in} - \theta$ ,  $j_{out} - \theta$  and  $h - \theta$  curves under loading and low speed conditions. Here, the mechanism behind this phenomenon is discussed. As we know,  $j_{in}$ ,  $j_{out}$  and  $h$  of the HD are calculated based on the positions of the FS and CS teeth in the meshing process, which can be seen in Figs. 2 and 8. Therefore, the abnormality of  $j_{in} - \theta$ ,  $j_{out} - \theta$  and  $h - \theta$  curves is likely caused by the abnormal motion characteristics of the FS teeth in the meshing process. To test this idea, the linear displacement  $d$  and angular displacement  $\beta$  of the marked FS tooth in the meshing process at different  $n_{in}$  and  $T_{out}$  are calculated by both the proposed and theoretical methods, and the results are shown in Fig. 12. The calculation process can refer to [10] and [14], and there is no space to cover them in detail. It is shown that the obtained  $d - \theta$  and  $\beta - \theta$  curves are very similar to  $j_{in} - \theta$ ,  $j_{out} - \theta$  and  $h - \theta$  curves shown in Fig. 10. At  $T_{out} = 0$  N·m, the translation motion of the marked FS tooth is smooth at any  $n_{in}$ , and small fluctuation exists in the rotation motion. However, the stick-slip phenomenon exists in both the translation and rotation motion of the marked FS tooth when  $T_{out} = 4$  N·m and  $n_{in} \leq 10$  r/min, and the critical speed of the stick-slip motion of the marked FS tooth increases to 20 r/min when  $T_{out} = 8$  N·m. The existence of the stick-slip motion of the FS teeth in the meshing process indicates the extremely complicated friction behavior in the meshing region under loading and low speed conditions [6], [49]–[51]. Since the friction between the FS and CS teeth in the meshing process cannot be measured nowadays [52]–[54], the origin of the stick-slip motion of the FS teeth in the meshing process should be further studied in the future work.

Based on above analyses, it can be concluded that the “stick-slip phenomenon” in the measured  $j_{in} - \theta$ ,  $j_{out} - \theta$  and  $h - \theta$  curves under loading and low speed conditions is caused by the existence of the stick-slip motion of the FS teeth in the meshing process. As shown in Fig. 2, since the theoretical model does not consider the contact and friction behavior between the FS and CS teeth in the meshing process, it cannot accurately predict the meshing characteristics of the HD under various operating conditions.

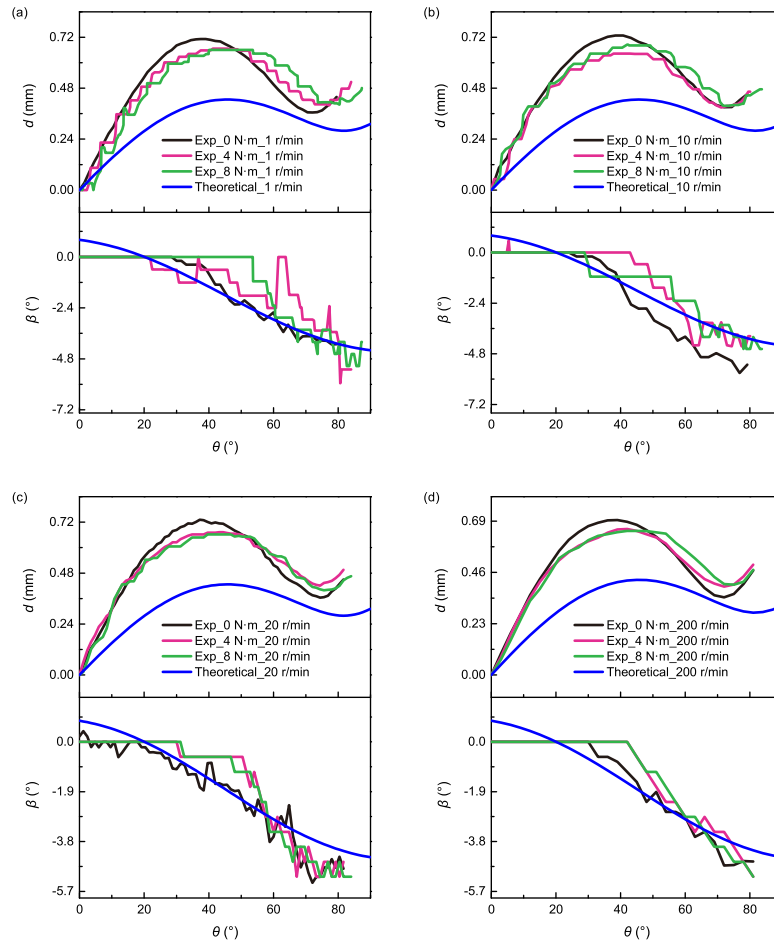


**FIGURE 12.** Variations of the calculated  $d$  and  $\beta$  by the proposed and theoretical methods with  $\theta$  at different  $n_{in}$ , and  $T_{out} = 0$  N-m, 4 N-m and 8 N-m in the experimental results. (a)  $n_{in} = 1$  r/min; (b)  $n_{in} = 10$  r/min; (c)  $n_{in} = 20$  r/min; (d)  $n_{in} = 200$  r/min.

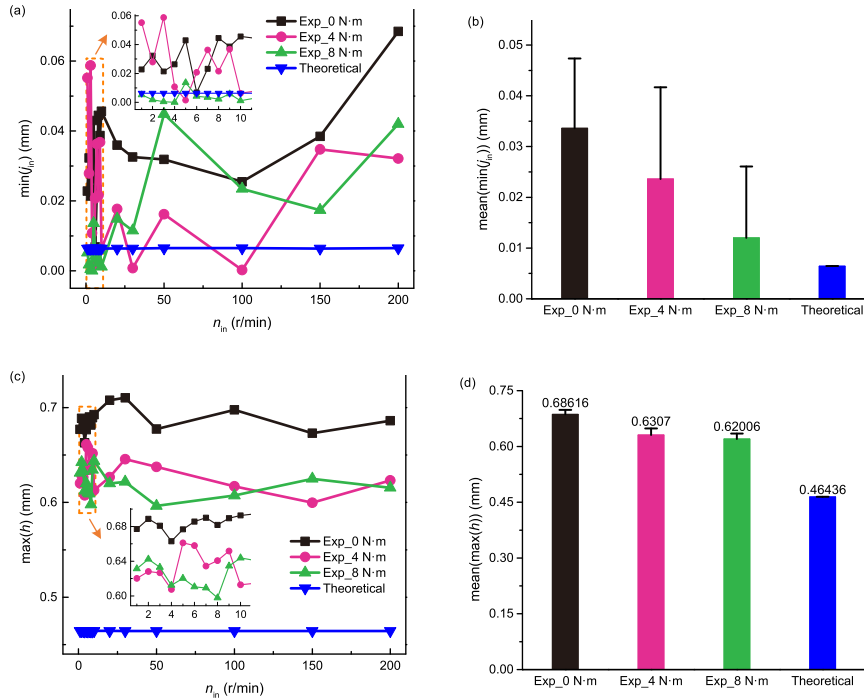
**C. EXPANSION AND VARIABILITY OF THE MINIMUM BACKLASH AND THE MAXIMUM DEPTH**

Fig. 10 also indicates that  $\min(j_{in})$ ,  $\min(j_{out})$  and  $\max(h)$  are greater than the theoretical ones, and they vary with  $n_{in}$  and  $T_{out}$ . Since the characteristic of  $j_{out}$  is similar to that of  $j_{in}$ , the effects of  $n_{in}$  and  $T_{out}$  on  $\min(j_{in})$  and  $\max(h)$  are examined, and the mechanisms behind them are further discussed. Figs. 13(a) and (c) show the comparison of the theoretical and measured  $\min(j_{in})$  and  $\max(h)$  at different  $n_{in}$  and  $T_{out}$ . Since the measured  $\min(j_{in})$  and  $\max(h)$  fluctuate with  $n_{in}$  at any  $T_{out}$ , their arithmetic means and standard deviations are calculated and shown in Figs. 14(b) and (d), respectively. The error bars are used to describe the fluctuation degrees of  $\min(j_{in})$  and  $\max(h)$  with  $n_{in}$ . The results show that  $\min(j_{in})$  fluctuates dramatically with the change of  $n_{in}$  except when  $T_{out} = 8$  N-m and  $n_{in} \leq 10$  r/min. Conversely,  $\max(h)$  is nearly not affected by  $n_{in}$  at any  $T_{out}$ . On the whole,  $\min(j_{in})$  decreases as  $T_{out}$  increases, and  $\max(h)$  under no-load condition is larger than that under loading condition.

The value of  $\max(h)$  is determined by the amplitude of  $w$  of the FS at the middle cross section of the tooth

rim [28], [32], [55]. Previous researches have revealed that the amplitude of

$w$  of the FS at the middle cross section of the tooth rim is nearly not affected by  $n_{in}$  and it is related to  $T_{out}$  [15], [28]. Thus, small fluctuation are seen in the measured  $\max(h) - n_{in}$  curves. Furthermore, it should be noticed that if  $\max(h)$  decreases as  $T_{out}$  increases, the gear engagement of the HD cannot be realized at higher  $T_{out}$ , and it can be seen that the  $\max(h)$  at  $T_{out} = 8$  N-m is a little smaller than that at  $T_{out} = 4$  N-m. Thus, it can be concluded that the amplitude of  $w$  of the FS at the middle cross section of the tooth rim first decreases and then tends to a constant as  $T_{out}$  increases. In addition, the maximum of  $d$  also depends on the amplitude of  $w$  of the FS at the middle cross section of the tooth rim, and Fig. 12 shows that the variation of the maximum of  $d$  with  $n_{in}$  and  $T_{out}$  are very similar to that of  $\max(h)$ . On the other hand, the value of  $\min(j_{in})$  is mainly determined by the shape of the meshing trajectory of the FS tooth [10]. According to (3), the meshing trajectory of the FS tooth is calculated by the deformation equation of the FS. Since the deformation characteristics of the FS are influenced by



**FIGURE 13.** Effects of  $n_{in}$  and  $T_{out}$  on  $\min(j_{in})$  and  $\max(h)$ . (a) and (c) Comparison of the theoretical and measured  $\min(j_{in})$  and  $\max(h)$  at different  $n_{in}$  and  $T_{out}$ ; (b) and (d) Comparison of the arithmetic means of the theoretical and measured  $\min(j_{in})$  and  $\max(h)$  at different  $T_{out}$ .

$n_{in}$  and  $T_{out}$  [15], [28], the fluctuation of  $\min(j_{in})$  with  $n_{in}$  suggests that the deformation shapes of the FS are irregular at different  $n_{in}$ . Moreover, other researchers also found that  $\min(j_{in})$  decreases as  $T_{out}$  increases [10], [16]. Since the deformation equation of the FS in the theoretical model does not cover the effects of  $n_{in}$  and  $T_{out}$ , the derived motion trajectory of the FS tooth in the meshing process is fixed, and the calculated  $\min(j_{in})$ ,  $\min(j_{out})$  and  $\max(h)$  are all constant.

## VI. CONCLUSION

A method for automated analysis of the meshing performance of the HD under various operating conditions is presented, and its performance is evaluated according to the computational accuracy and efficiency. The results show that the ratios of the CSU of the calculated meshing parameters to their estimated values are close to zero, and the designed position tracking algorithm for the FS teeth takes about 1.59 seconds per video frame when running on a laptop of 2.6GHz CPU and 12GB RAM. Further, the validity and advantages of the proposed method are demonstrated through comparing with the previous method. It is shown that the overall variation tendencies of  $j_{in}$ ,  $j_{out}$  and  $h$  of the HD obtained by two methods are consistent. However, the conventional method cannot replicate the effects of  $n_{in}$  and  $T_{out}$  on the meshing performance of the HD, which are summarized as follows: 1)  $\theta_{total}$  is actually less than half of the meshing period, and it increases as  $T_{out}$  increases; 2)  $j_{in} - \theta$ ,  $j_{out} - \theta$  and  $h - \theta$  curves are smooth under no-load condition, whereas they show the “stick-slip phenomenon” under loading and

low speed conditions; 3)  $\min(j_{in})$  fluctuates with  $n_{in}$ , and it decreases as  $T_{out}$  increases; 4)  $\max(h)$  nearly keeps constant at different  $n_{in}$ , and it first decreases and then tends to a constant as  $T_{out}$  increases. Last, the mechanisms behind these phenomena and the deficiencies of the theoretical method are discussed. Our results reveal that the stick-slip motion of the FS teeth in the meshing process results in the abnormal variations of  $j_{in}$ ,  $j_{out}$  and  $h$  with  $\theta$  at low  $n_{in}$ . Moreover, the amplitude of  $w$  of the FS at the middle cross section of the tooth rim first decreases and then tends to a constant as  $T_{out}$  increases. However, the theoretical model does not consider the contact and friction behavior between the FS and CS teeth in the meshing process, and the effects of  $n_{in}$  and  $T_{out}$  on the deformation characteristics of the FS are also ignored.

Our method provides an effective tool for manufacturers to examine the meshing performance of the HD, and the obtained results can be used as references for improvement of the theoretical models and design of new tooth profiles of the HD. However, the proposed method is only performed under dry friction condition in this work, and the grease and solid lubricants are usually used in the HD. Consequently, designing an improved position tracking algorithm to effectively classify the teeth and lubricants in the meshing images of the HD will be the focus of our future work.

## REFERENCES

- [1] C. W. Musser, “Strain wave gearing,” U.S. Patent 2906 143, Sep. 29, 1959.
- [2] R. Slatter and G. Mackrell, “Harmonic drives in tune with robots,” *Ind. Robot, Int. J.*, vol. 21, no. 3, pp. 24–28, 1994.



- [3] G. Liu, Y. Liu, H. Zhang, X. Gao, J. Yuan, and W. Zheng, "The Kapvik Robotic Mast: An Innovative Onboard Robotic Arm for Planetary Exploration Rovers," *IEEE Robot. Autom. Mag.*, vol. 22, no. 1, pp. 34–44, Mar. 2015.
- [4] B.-J. Jung, B. Kim, J. C. Koo, H. R. Choi, and H. Moon, "Joint torque sensor embedded in harmonic drive using order tracking method for robotic application," *IEEE/ASME Trans. Mechatronics*, vol. 22, no. 4, pp. 1594–1599, Aug. 2017.
- [5] Z. Shi, Y. Li, and G. Liu, "Adaptive torque estimation of robot joint with harmonic drive transmission," *Mech. Syst. Signal Process.*, vol. 96, pp. 1–15, Nov. 2017.
- [6] C. W. Kennedy and J. P. Desai, "Modeling and control of the Mitsubishi PA-10 robot arm harmonic drive system," *IEEE/ASME Trans. Mechatronics*, vol. 10, no. 3, pp. 263–274, Jun. 2005.
- [7] N. M. Kircanski and A. A. Goldenberg, "An experimental study of nonlinear stiffness, hysteresis, and friction effects in robot joints with harmonic drives and torque sensors," *Int. J. Robot. Res.*, vol. 16, no. 2, pp. 214–239, 1997.
- [8] P. S. Gandhi and F. H. Ghorbel, "Closed-loop compensation of kinematic error in harmonic drives for precision control applications," *IEEE Trans. Control Syst. Technol.*, vol. 10, no. 6, pp. 759–768, Nov. 2002.
- [9] R. Dhauadi, F. H. Ghorbel, and P. S. Gandhi, "A new dynamic model of hysteresis in harmonic drives," *IEEE Trans. Ind. Electron.*, vol. 50, no. 6, pp. 1165–1171, Dec. 2003.
- [10] M. N. Ivanov, *The Harmonic Drive*, Beijing, China: Defense Industry Press, 1987, pp. 1–96.
- [11] X. Chen, Y. Liu, J. Xing, S. Lin, and W. Xu, "The parametric design of double-circular-arc tooth profile and its influence on the functional backlash of harmonic drive," *Mech. Mach. Theory*, vol. 73, pp. 1–24, Mar. 2014.
- [12] Y. T. Oh, "Influence of the joint angular characteristics on the accuracy of industrial robots," *Ind. Robot, Int. J.*, vol. 38, no. 4, pp. 406–418, 2011.
- [13] M. Ruderman, F. Hoffmann, and T. Bertram, "Modeling and identification of elastic robot joints with hysteresis and backlash," *IEEE Trans. Ind. Electron.*, vol. 56, no. 10, pp. 3840–3847, Oct. 2009.
- [14] D. Ma, J. Wu, and S. Yan, "A method for detection and quantification of meshing characteristics of harmonic drive gears using computer vision," *Sci. China-Technol. Sci.*, vol. 59, no. 9, pp. 1305–1319, Sep. 2016.
- [15] H. M. Dong, "Study on kinematics and meshing characteristic of harmonic gear drives based on the deformation function of the flexspline," Ph.D. dissertation, School Mech. Eng., Dalian Univ. Technol., Dalian, China, 2008.
- [16] Y. W. Shen and Q. T. Ye, *Theory and Design of Harmonic Drive*, Beijing, China: China Machine Press, 1985, pp. 1–175.
- [17] K. Kondo and J. Takada, "Study on tooth profiles of the harmonic drive," *J. Mech. Des.*, vol. 112, no. 1, pp. 131–137, 1990.
- [18] H. B. Xin, "A new method for research on engagement principle of harmonic drive," *China Mech. Eng.*, vol. 13, no. 3, pp. 181–183, Feb. 2002.
- [19] J. X. Wang, X. X. Zhou, J. Y. Li, K. Xiao, and G. W. Zhou, "Three dimensional profile design of cup harmonic drive with double-circular-arc common-tangent tooth profile," *J. Zhejiang Univ. (Eng. Sci.)*, vol. 50, no. 4, pp. 616–713, Apr. 2016.
- [20] Y. Yang, J. X. Wang, Q. H. Zhou, J. X. Zhu, and W. Y. Yang, "Exact solution for conjugate profiles of zero backlash harmonic drives with elliptical cam wave generators," *J. Central South Univ. (Sci. Technol.)*, vol. 48, no. 12, pp. 3231–3238, 2017.
- [21] H. Dong, K.-L. Ting, and D. L. Wang, "Kinematic fundamentals of planar harmonic drives," *J. Mech. Des.*, vol. 133, no. 1, p. 011007, 2011.
- [22] H. Dong, D. Wang, and K.-L. Ting, "Kinematic effect of the compliant cup in harmonic drives," *J. Mech. Des.*, vol. 133, no. 5, p. 051004, 2011.
- [23] J. X. Wang, P. Yuan, C. L. Tan, Y. Q. He, J. Y. Li, and K. Xiao, "Spatial tooth profile design of harmonic drive by rack approximation method," *J. Jilin Univ. (Eng. Technol. Ed.)*, vol. 47, no. 4, pp. 1121–1129, 2017.
- [24] S. Ishikawa, "Tooth profile of spline of strain wave gearing," U.S. Patent 4823 638, Apr. 25, 1989.
- [25] D. Leon, N. Arzola, and A. Tovar, "Statistical analysis of the influence of tooth geometry in the performance of a harmonic drive," *J. Braz. Soc. Mech. Sci. Eng.*, vol. 37, no. 2, pp. 723–735, Mar. 2015.
- [26] V. Sahoo and R. Maiti, "Evidence of secondary tooth contact in harmonic drive, with involute toothed gear pair, through experimental and finite element analyses of stresses in flex-gear cup," *Proc. Inst. Mech. Eng. C, J. Mech. Eng. Sci.*, vol. 232, no. 2, pp. 341–357, Jan. 2018.
- [27] V. Sahoo and R. Maiti, "Load sharing by tooth pairs in involute toothed harmonic drive with conventional wave generator cam," *Meccanica*, vol. 53, nos. 1–2, pp. 373–394, Jan. 2018.
- [28] D. H. Ma, J. N. Wu, T. Liu, and S. Z. Yan, "Deformation analysis of the flexspline of harmonic drive gears considering the driving speed effect using laser sensors," *Sci. China-Technol. Sci.*, vol. 60, no. 8, pp. 1175–1187, Aug. 2017.
- [29] Q. Xiang and Z.-N. Yin, "Investigation of temperature effect on stress of flexspline," *Appl. Math. Mech.*, vol. 35, no. 6, pp. 791–798, 2014.
- [30] J. Pacana, W. Witkowski, and J. Mucha, "FEM analysis of stress distribution in the hermetic harmonic drive flexspline," *Strength Mater.*, vol. 49, no. 3, pp. 388–398, May 2017.
- [31] Y.-C. Chen, Y.-H. Cheng, J.-T. Tseng, and K.-J. Hsieh, "Study of a harmonic drive with involute profile flexspline by two-dimensional finite element analysis," *Eng. Comput.*, vol. 34, no. 7, pp. 2107–2130, 2017.
- [32] X. Chen, Y. Liu, J. Xing, S. Lin, and M. Ma, "A novel method based on mechanical analysis for the stretch of the neutral line of the flexspline cup of a harmonic drive," *Mech. Mach. Theory*, vol. 76, pp. 1–19, Jun. 2014.
- [33] O. Kayabasi and F. Erzincanli, "Shape optimization of tooth profile of a flexspline for a harmonic drive by finite element modelling," *Mater. Des.*, vol. 28, no. 2, pp. 441–447, 2007.
- [34] H. Zhang, S. Ahmad, and G. Liu, "Modeling of torsional compliance and hysteresis behaviors in harmonic drives," *IEEE/ASME Trans. Mechatronics*, vol. 20, no. 1, pp. 178–185, Feb. 2015.
- [35] J. R. Xie, "Meshing analysis method of the harmonic drive gears with elliptical cam wave generators," *Opt. Precis. Eng.*, no. 3, pp. 33–40, 1980.
- [36] C. Zou, T. Tao, G. D. Jiang, and X. S. Mei, "Deformation and stress analysis of short flexspline in the harmonic drive system with load," in *Proc. IEEE Int. Conf. Mechatronics Autom.*, Aug. 2013, pp. 676–680.
- [37] M. Liang and X. Hu, "Recurrent convolutional neural network for object recognition," in *Proc. IEEE Conf. Comput. Vis. Pattern Recognit.*, Jun. 2015, pp. 3367–3375.
- [38] J. Canny, "A computational approach to edge detection," *IEEE Trans. Pattern Anal. Mach. Intell.*, vol. 8, no. 6, pp. 679–698, Nov. 1986.
- [39] R. C. Gonzalez and R. E. Woods, *Digital Image Processing*, 2nd ed. Upper Saddle River, NJ, USA: Prentice-Hall, 2002, pp. 520–560.
- [40] H. Bay, A. Ess, T. Tuytelaars, and L. Van Gool, "Speeded-up robust features (SURF)," *Comput. Vis. Image Understand.*, vol. 110, no. 3, pp. 346–359, 2008.
- [41] R. Hartley and A. Zisserman, *Multiple View Geometry in Computer Vision*, 2nd ed. Cambridge, U.K.: Cambridge Univ. Press, 2004, pp. 25–64.
- [42] P. H. S. Torr and A. Zisserman, "MLESAC: A new robust estimator with application to estimating image geometry," *Comput. Vis. Image Understand.*, vol. 78, no. 1, pp. 138–156, 2000.
- [43] S. Shirmohammadi and A. Ferrero, "Camera as the instrument: The rising trend of vision based measurement," *IEEE Instrum. Meas. Mag.*, vol. 17, no. 3, pp. 41–47, Jun. 2014.
- [44] S. L. Wu and J. Zhang, *Error Analysis and Data Processing*. Beijing, China: Tsinghua Univ. Press, 2010, pp. 55–60 and 175–185.
- [45] I. H. Lira and W. Wöger, "The evaluation of standard uncertainty in the presence of limited resolution of indicating devices," *Meas. Sci. Technol.*, vol. 8, no. 4, pp. 441–443, 1997.
- [46] K. Ueura, Y. Kiyosawa, J. Kurogi, S. Kanai, H. Miyaba, and K. Maniwa, "Tribological aspects of a strain wave gearing system with specific reference to its space application," *Proc. Inst. Mech. Eng., J, J. Eng. Tribol.*, vol. 222, no. 8, pp. 1051–1061, 2008.
- [47] J.-Y. Li, J.-X. Wang, G.-W. Zhou, W. Pu, and Z.-H. Wang, "Accelerated life testing of harmonic driver in space lubrication," *Proc. Inst. Mech. Eng., J, J. Eng. Tribol.*, vol. 229, no. 12, pp. 1491–1502, 2015.
- [48] J. F. Ma, C. Li, Y. C. Luo, and L. L. Cui, "Simulation of meshing characteristics of harmonic reducer and experimental verification," *Adv. Mech. Eng.*, vol. 10, no. 3, pp. 1–9, 2018.
- [49] B. Han, J. Ma, and H. Li, "Research on nonlinear friction compensation of harmonic drive in gimbal servo-system of DGCMG," *Int. J. Control Autom. Syst.*, vol. 14, no. 3, pp. 779–786, Jun. 2016.
- [50] M. Ruderman, F. Hoffmann, and T. Bertram, "Identification and compensation of stick-slip friction in harmonic-drive gear transmission," in *Proc. Int. Conf. Noise Vib. Eng.*, 2008, pp. 949–960.
- [51] H. B. Liao, S. X. Fan, and D. P. Fan, "Friction compensation of harmonic gear based on location relationship," *Proc. Inst. Mech. Eng. I, J. Syst. Control Eng.*, vol. 230, no. 8, pp. 695–705, Sep. 2016.
- [52] D. H. Ma, J. N. Wu, and S. Z. Yan, "Advances in researches of dynamic models in harmonic drive system," *China Sciencepaper*, vol. 10, no. 16, pp. 1983–1990, 2015.

- [53] D. H. Ma, Z. Wu, and D. Y. Lin, "Review on testing methods of tooth surface friction of the gear system," *China Sciencepaper*, vol. 12, no. 4, pp. 361–366, 2017.
- [54] T. D. Tuttle and W. P. Seering, "A nonlinear model of a harmonic drive gear transmission," *IEEE Trans. Robot. Autom.*, vol. 12, no. 3, pp. 368–374, Jun. 1996.
- [55] C. J. Liu, L. J. Chen, and C. Wei, "Deformation and stress analysis of flexspline in harmonic drive based on finite element method," *Int. J. Sci.*, vol. 2, no. 1, pp. 96–100, 2015.



**DONGHUI MA** received the B.S. degree in mechanical design, manufacturing and automation from the School of Technology, Beijing Forestry University, Beijing, China, in 2014. He is currently pursuing the Ph.D. degree in mechanical engineering with the Department of Mechanical Engineering, Tsinghua University, Beijing.

His current research interests include the fundamental studies of the kinematic and dynamic behavior in the meshing process of harmonic drive gears based on artificial intelligence and optical measurement techniques and the precise modeling and control of harmonic drive systems used in the industrial and space robots.



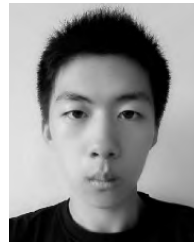
**RUI WANG** is currently pursuing the B.Eng. degree in mechanical engineering with the Department of Mechanical Engineering, Tsinghua University, Beijing, China.

His current research interests include the advanced measurement techniques for harmonic drive gears and the precise modeling of harmonic drive systems used in the industrial and space robots.



**PENGFEE RAO** is currently pursuing the B.Eng. degree in mechanical engineering with the Department of Mechanical Engineering, Tsinghua University, Beijing, China.

His current research interests include the image processing and computer vision, and their applications in harmonic drive gears.



**RUOMIN SUI** is currently pursuing the B.Eng. degree in mechanical engineering with the Department of Mechanical Engineering, Tsinghua University, Beijing, China.

His current research interests include the advanced measurement techniques for harmonic drive gears and the precise modeling of harmonic drive systems used in the industrial and space robots.



**SHAOZE YAN** received the B.S., M.S., and Ph.D. degrees from the School of Mechanical Engineering, Tianjin University, Tianjin, China, in 1987, 1990, and 1996, respectively.

He is currently a Professor with the State Key Laboratory of Tribology, Department of Mechanical Engineering, Tsinghua University, Beijing, China. His current research interests include the dynamics of mechanical system with clearance, impact, and contact, the reliability analysis of mechanical system, and the insect bionics and intelligent structure.

...